Measurements of weak and moderate oblique shock-vortex interactions in supersonic flow

Jack Thompson, Ramez M. Kiriakos ⬤, Arastou Pournadali Khamseh ⬤, and Edward P. DeMauro[*]
Rutgers, The State University of New Jersey, Piscataway, New Jersey 08854, USA

Experiments were performed to quantify the interaction of a streamwise vortex with a series of oblique shock waves using stereoscopic particle image velocimetry. For these experiments, the streamwise vortex was created using a diamond-shaped, finite-span wing, pitched to one of two angles of attack ($\alpha = 5°, 10°$). Downstream of the wing, the streamwise vortex encountered a two-dimensional oblique shock, generated by a wedge ($\theta = 15°, 20°, 25°$), resulting in a series of weak and moderate oblique shock-vortex interactions. While only moderate interactions produced a conical shock distortion, all interactions resulted in appreciable changes to the flow field downstream of the shock. These changes were reflected in increased velocity deficits and induced rotational motion; in the case of moderate interactions, increased turbulence kinetic energy was also apparent.

I. INTRODUCTION

Precision guidance of missiles requires that control surfaces respond in a desirable and repeatable way. As many missiles make use of upstream-mounted canards, wing-tip vortices can shed downstream, with the potential to negatively impact rear control surfaces [1–3]. In supersonic flight conditions, these vortices will encounter oblique shocks about a control surface, giving rise to a complex oblique shock-vortex interaction (OSVI) [4,5]. Unwanted aerodynamic loads may develop, leading to a loss in precision control, which is unacceptable for reliable performance [1,6–8]. Although many computational studies have been performed to understand the flow field of shock-vortex interactions, there is a lack of quantitative experimental data within the open literature, leading to many simulations and theoretical models remaining unvalidated by experiments [8–10]. For this reason, there exists a real need to provide meaningful, quantitative, validation data associated with OSVI to improve predictive capabilities.

Much of what is currently known about these interactions is limited to normal shock-vortex interactions (NSVI) [4]. In general, NSVI are considered to be axisymmetric interactions where the shock primarily influences the axial velocity component, leaving the tangential velocity components relatively in tact. Two potential outcomes can arise in NSVI: a weak interaction where the vortex continues downstream or a strong interaction that results in vortex breakdown and the formation of a conical shock structure at the point of interaction [11–13]. One key feature presenting evidence of vortex breakdown is the presence of reverse axial flow, along with expansion of the vortex core in a manner similar to what is seen with incompressible vortex breakdown [11]. In contrast to NSVI, OSVI see relatively weaker pressure jumps due to the decreased shock angle. As the vortex approaches the oblique shock, the vortex's axis is no longer perpendicular to the shock, such that the interaction is not axisymmetric. Similarly to NSVI, OSVI are also defined as weak and strong; however, moderate interactions are also possible where deformation of the shock is observed without

---

[*]Corresponding author: edward.demauro@rutgers.edu

the signs of vortex breakdown [14]. Finally, because the vortex may survive OSVI, it will likely be distorted but continue downstream. In this instance, the core of the vortex changes direction to be parallel to the deflected flow [7].

Existing experimental data on OSVI were largely obtained using predominantly qualitative measurements, although Pitot probe and surface pressure measurements are reported. For example, Kalkhoran *et al.* [15] used Schlieren imaging to perform an initial study of the OSVI interaction created from a wakelike vortex. A three-dimensional conical shock structure was identified at the point of vortex interaction, similarly to what was observed in NSVI, which the authors attributed to the vortex's velocity deficit. Smart and Kalkhoran [6] used Schlieren imaging to study the influence of shock strength and swirl ratio on the potential for vortex breakdown. They observed moderate interactions that resulted in the vortex continuing to travel downstream of the oblique shock, at times even impacting the wedge surface. Kalkhoran and Sforza [16] measured changes to surface pressure on an airfoil due to OSVI, as a function of the relative height of the vortex above the leading edge. It was found that the greatest influence on the aerodynamic loading occurred when the vortex impinged directly on the leading edge.

Following on these measurements, Smart *et al.* [7] used Schlieren imaging and planar laser scattering to attempt to study a strong OSVI with a wakelike streamwise vortex. While they could not determine the presence of reverse axial flow, they were able to observe the formation of the conical shock structure. They argued that, since the vortex had a wakelike profile, the Mach number at the core was lowest, where the conical shock was locally normal. For this reason, a region of subsonic flow is created within the core of the vortex. The vortex was seen to expand and then change direction, parallel to the wedge surface. Finally, a unique set of experiments were performed by Leopold *et al.* [5] and Klaas *et al.* [17] using Laser doppler velocimetry (LDV) and particle image velocimetry (PIV) to study the interaction. Klaas *et al.* [17] observed the changes induced to the swirl ratio of the vortex due to passage through the oblique shock, while Leopold *et al.* [5] used LDV to observe unsteadiness in the interaction. In both instances, however, the data were two dimensional, obtained for a three-dimensional interaction.

This paper presents work examining the interaction of a streamwise vortex with an oblique shock wave. Using stereoscopic particle image velocimetry, this study looks to quantify the state of the on-coming vortex, along with measuring the changes induced to the shock due to interaction with the vortex. For these experiments, the vortex is a wing-tip vortex generated by a finite-span wing placed upstream of the wedge. Two swirl ratios, corresponding to two angles of attack, are investigated. The oblique shock wave is varied in strength by altering the deflection angle. The goal of this work is to examine flow field associated with weak and moderate OSVI, observing how the shock and the vortex are mutually influenced by the interaction, while also providing nonintrusive, quantitative measurements of the associated flow field.

II. EXPERIMENTAL SETUP

A. Rutgers University Supersonic Wind Tunnel

Experiments were performed at Rutgers University's Emil Buehler Supersonic Wind Tunnel (SWT), which is a blowdown-to-atmosphere cold flow facility. The tunnel is equipped with an asymmetric one-sided nozzle, expanding the flow to a nominal freestream Mach number of 3.4 at the entrance to the test section. The tunnel is supplied with dried, compressed air at 16.6 MPa, stored in tanks with a total volume of 8 m^3. The test section of the wind tunnel has a cross-sectional area measuring about 15×15 cm^2, with windows available on all four surfaces to provide optical access. Within the test section, a turbulent boundary layer develops naturally, resulting in a 99% thickness of $\delta_{99} = 16.4$ mm. Additionally, the displacement and momentum thicknesses of SWT are $\delta_1 = 6.4$ mm and $\delta_2 = 1.0$ mm, respectively. The average stagnation pressure and temperature were 1.00 MPa and 297 K, respectively, where T_0 is set by the outside air temperature about the storage tanks. The tunnel was operated such that freestream Mach number at the entrance
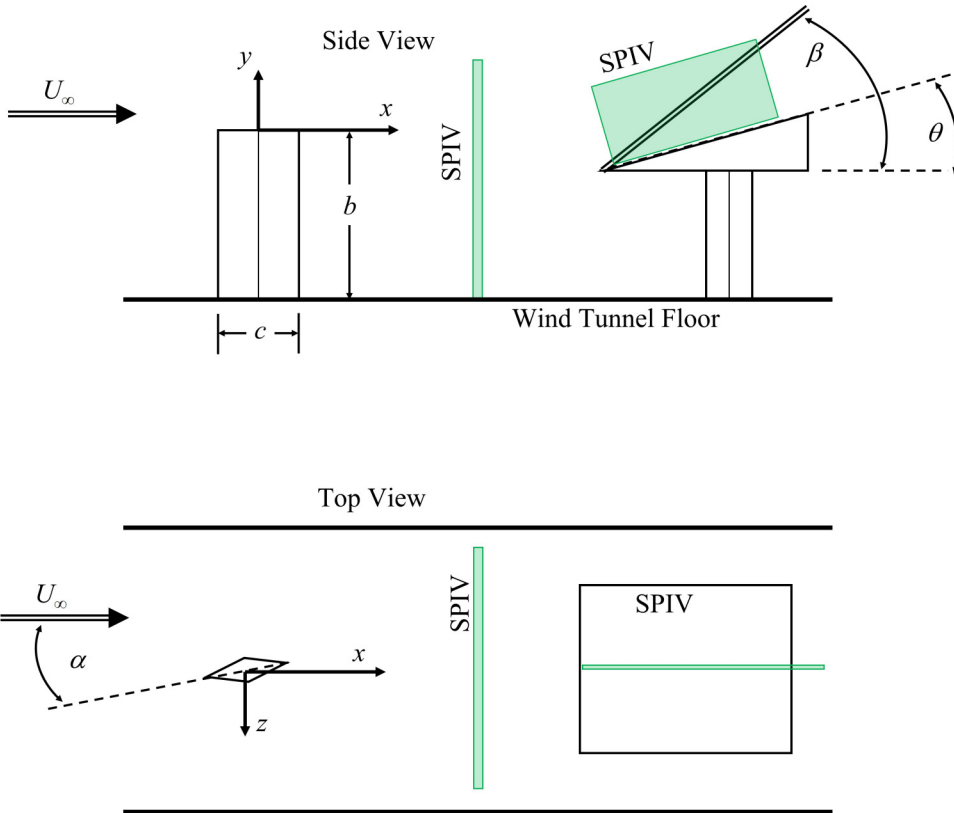
FIG. 1. Schematic of the OSVI experimental setup. Drawing is not to scale.

of the test section measured 2.9. For the conditions, this resulted in a freestream velocity of $U_\infty = 612$ m/s ($q_\infty = 186$ kPa) and a unit Reynolds number of 7.91×10^7/m. Typical run times at these conditions are approximately 15–20 s.

B. Vortex generation method and shock generators

The oblique shock-vortex interactions are created using a finite wing (with a free-end) placed upstream of shock-generating wedges, as shown in Fig. 1. The finite wing is built from a symmetric diamond shape, with a half-angle of 16°, a chord (c) of 63.5 mm, and a wingspan (b) of 75 mm. The coordinate system for the experiments is defined as in Fig. 1, with respect to the midchord and wing tip. For a given angle of attack, α, the resultant pressure difference about the wing gives rise to the creation of a streamwise wingtip vortex that propagates downstream. This vortex formation method results in a wakelike profile, similarly to those created in studies by Kalkhoran et al. [15], Kalkhoran and Sforza [16], Smart et al. [18], and Smart et al. [7]. Two angles of attack, i.e., two vortices of different swirl strengths (τ) are employed: $\alpha = 5°$ and $\alpha = 10°$.

Three shock generator wedges are used with nominal deflection angles of $\theta = 15°$, $\theta = 20°$, and $\theta = 25°$. Each wedge is rectangular, measuring 76.7 mm in length by 57.2 mm in width. The leading edges of the shock generators are located approximately $2.6c$ downstream of the wing's midchord, with slight variation in streamwise location due to changing deflection angle. This will be shown explicitly in the data set. In addition, the wedges are painted matte black to minimize specular reflection of the laser sheet. An assessment of the baseline oblique shocks is presented to compare against theoretical values.

C. Stereoscopic particle image velocimetry

Stereoscopic particle image velocimetry (SPIV) measurements were performed using a LaVision DaVis v8.4 system. The light source for this system is a Quantel Evergreen 200 mJ/pulse, double-pulsed Nd:YAG laser, producing a wavelength of $\lambda = 532$ nm, operating at a repetition rate of 15 Hz. The time delay between the two laser pulses was $\delta t = 0.5$ μs, to permit for adequate particle displacement. The laser sheet was expanded, using typical sheet-forming optics, and directed into the wind tunnel, through the floor of the test section. Burn measurements were performed to confirm a sheet thickness of about 1.5 mm. For measurements of the oblique shocks, the laser sheet was pointed directly at the wedge surface. Care was taken to avoid the presence of laser reflections within the data set by slightly offsetting the data set from the surface of the wedge and carefully adjusting the camera viewing angles.

The SPIV system was triggered internally using a LaVision Programmable Timing Unit PTU X. Images were obtained using a pair of LaVision Imager scientific complementary metal-oxide-semiconductor (sCMOS) cameras, with Scheimpflug adapters. The sCMOS cameras have a resolution of 2560×2160 pixels, digitized to 16 bits. The cameras are equipped with a pair of 200-mm Nikon Nikkor lenses. In this experiment, the cameras were calibrated using a 58 mm $\times$ 58 mm calibration target. A self-calibration procedure was applied, followed by performing a multipass processing algorithm. For the multipass procedure, the first pass used a 64×64 pixels window with 50% overlap, followed by two passes of 48×48 pixels windows with 75% overlap.

DaVis employs correlation statistics method to find the uncertainty of PIV displacement field, which accounts for various sources of errors such as pixel noise, out-of-plane motion, seeding density, and particle image size [19]. The uncertainty can vary spatially throughout different regions of the field, owing to optical clarity or specific flow phenomena within these regions. For the vortex cross-stream measurements, the maximum precision uncertainties within the core were measured to be $0.003U_\infty$, $0.004U_\infty$, and $0.003U_\infty$ for U, V, and W, respectively. For the OSVI measurements, the maximum precision uncertainties were measured to be $0.007U_\infty$, $0.012U_\infty$, and $0.014U_\infty$ for U, V, and W, respectively.

Seeding was provided using a ViCount thermal smoke generator, which is specified to produce particles with a diameter of 0.2–0.3 μm, using mineral oil as its base. Seed was introduced into the wind tunnel at the stagnation chamber, upstream of the blast plate; this allows for the seed to be fully distributed within the flow by the entrance of the test section. The relaxation time of the particles (τ_p) has been previously measured by Panco and DeMauro [20], where they presented a Stokes number (Stk) based on the wind tunnel's boundary layer thickness as Stk $= \tau_p \delta_{99}/U_\infty = 0.09$. These measurements were obtained by measuring the particle response to an oblique shock; this value is cited here simply to provide the value of τ_p used in estimation of the Stokes number in the subsequent section. The first part of this paper involves estimation of a Stokes number associated with the flow field under investigation, using the response time presented here. It should be noted that the Stokes number is properly a field variable that depends on the specific feature of interest. For this study, the Stokes number was defined using the vorticity of the (ensemble-averaged) streamwise vortices, as will be discussed further in the following sections.

III. RESULTS AND DISCUSSION

To build a quantitative discussion of the full oblique shock vortex interaction, both the vortex and shock should be defined. It has been suggested that the streamwise momentum, the swirl strength, and thus the Mach profile of the incoming vortex play a critical role in shaping the shock interaction and potential vortex breakdown [4,7,21,22]. The first set of experiments were dedicated to quantifying the vortices alone, without shocks present. Cross-stream measurements of the wing-tip vortex were performed at $x/c = 1.5$, downstream of the wing's midchord location, to accomplish two goals: (1) quantification of the vortex and (2) investigate the potential for
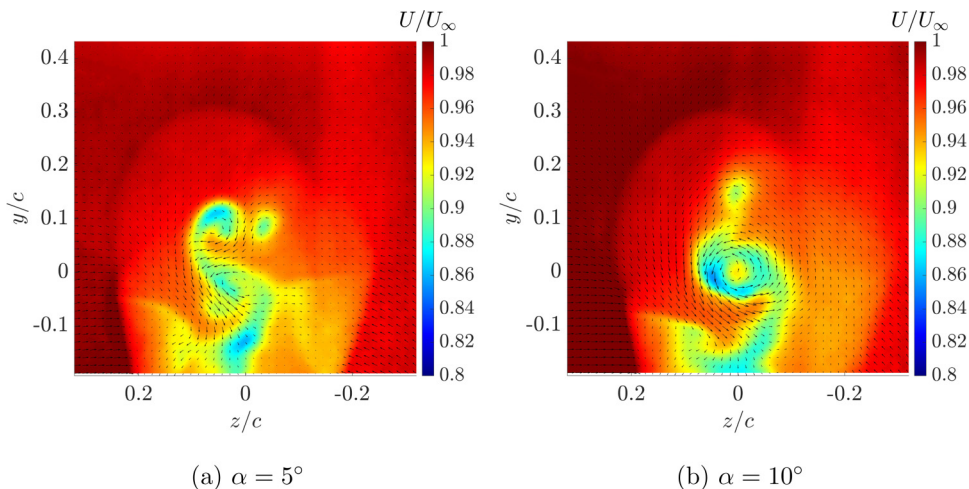
FIG. 2. Color contours of streamwise velocity with in-plane velocity vectors (ensemble-average) of the wing-tip vortex, obtained at $x/c = 1.5$: (a) $\alpha = 5°$ and (b) $\alpha = 10°$.

particle dropout. This section further quantifies the particle Stokes number for the experiment, using vorticity as a timescale.

A. Quantification of the wing-tip vortex

Color contours of ensemble-averaged streamwise velocity with superposed in-plane velocity vectors are shown in Fig. 2. These measurements were obtained within the near-wake of the wing-tip, as indicated by the tails seen about the vortices. The primary flow component, U, is directed through the page toward the reader, meaning that timing was crucial to ensure that particles did not vacate the laser sheet before the second raw image could be obtained. The resultant vector resolution for these images is about 0.23 mm/vector. In these images, the coordinates follow the convention given in Fig. 1, where the origin is placed at midchord; however, the vortex center is assumed to be the height of the free-end. This point will be addressed in the next section. In both images, a noticeable velocity deficit can be seen, indicating that the wing-tip produced a wakelike vortex profile. The $\alpha = 10°$ vortex, as shown in Fig. 2(b) has a more well-defined shape compared to its $\alpha = 5°$ counterpart shown in Fig. 2(a), as evidenced by the clear rotational motion seen within the in-plane vectors. The features of this flow show large qualitative agreement with simulations performed by Borisov *et al.* [23] and Rizzetta [24]. In general, the formation of the wing tip vortex follows the same basic mechanisms seen with the incompressible case. A pressure differential is created by the wing pitched to an angle of attack, due to the presence of shock and expansion waves. At the wing-tip, flow moves freely from the pressure side of the wing, wrapping around the tip toward the suction side.

One reason for performing these cross-plane measurements of the vortex was to assess the potential for particle dropout. Lecuona *et al.* [25], looking at incompressible vortices seeded with tracer particles, indicated that particle seeding is more susceptible to radial flow velocities than azimuthal flow velocities; the result is that particles tend to follow a spiralling motion away from the center of a vortex. As vortices increase in strength, particle seeding will become weaker toward the core, and eventually there can be too few particles to resolve even the azimuthal velocity.

Likewise, particle lag can result in a change to the measured velocities. The major influence of particle lag would be seen in inaccurate measurements of the azimuthal and radial velocities. In comparing the swirl values in this study with those found in Kalkhoran and Smart [4], the values reported here do appear somewhat smaller for similar angles of attack. This could be associated

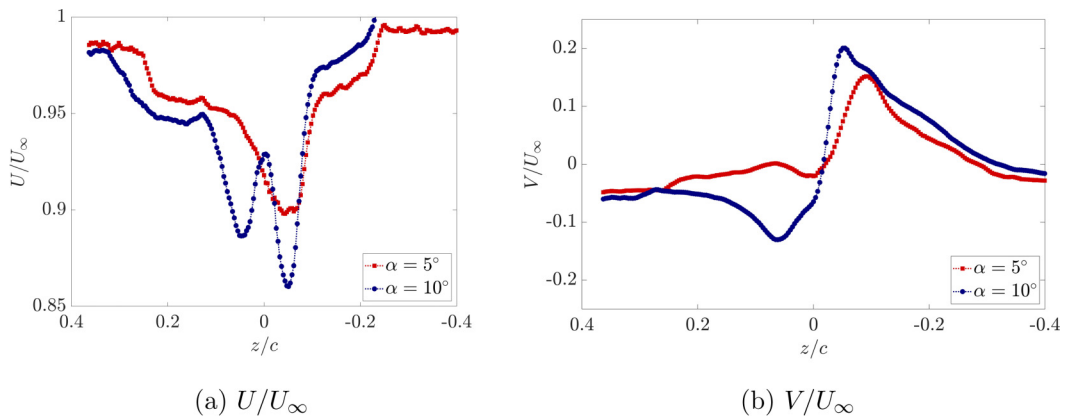(a) U/U_∞ (b) V/U_∞

FIG. 3. Horizontal distributions of (a) streamwise and (b) vertical obtained through the centerline of the vortex.

with the particle lag. Estimation of the bias associated with particle lag is a nontrivial task. Birch and Martin [26] attempted to theoretically estimate the error due to particle lag associated with a Batchelor vortex. While validation of their results proved to be challenging, they predicted that the radial velocity appears to be much more sensitive to particle lag than the azimuthal velocity, in agreement with Lecuona *et al.* [25]. For this reason, it is possible that the shape of the vortex could be influenced by the particle lag.

An additional concern is the potential for peak locking within regions of a flow where only smaller-scale particles remain. Referring to work by Christensen [27], the mean velocities shown here should be relatively insensitive to peak locking, whereas uncertainties will accumulate within turbulent statistics and the RMS values of vorticity. For example, severe peak locking can lead to large uncertainty in the vorticity RMS as high as 30–40% [28]. In addition, peak locking can also lead to underestimating the magnitude of turbulent quantities [27]. As the estimation of the vortex swirl is based on measurements of mean velocities, it is believed that the swirl ratios should be relatively insensitive to peak locking. Regardless, the estimation of the Stokes number in these data, using the vorticity, would likely not be underestimated due to the mean vorticity itself expected to be weakly influenced by peak locking [27].

Figure 3 shows distributions of the streamwise and vertical velocity components for the two vortices. Both distributions were obtained along horizontal lines through the center of the vortex. For this reason, the vertical velocity component at this location simultaneously functions as a measure of the azimuthal velocity. The profiles are asymmetric, which is a feature of wing-tip vortices noted in previous literature [18]. In general, both profiles appear to represent wakelike vortices. Interestingly, however, the $\alpha = 10°$ vortex shows a markedly different profile than the $\alpha = 5°$ vortex, due to the presence of a secondary peak within the vortex core.

A double peak within the axial velocity profile has been occasionally seen within other literature; however, much of the existing literature is restricted to low-speed aerodynamic flows. Regardless, the expectation is that certain general features should be similar, given that the formation mechanism is inherently the same, namely a pressure gradient due to the lift-generation process. Devenport *et al.* [29] and Lee and Pereira [30] both observed a small double peak at 10 and 5 chord lengths, respectively, downstream of the generator. In both situations, the shape of the axial velocity distribution was attributed to the angle of attack of the wing, along with the shape of the end cap. Chigier and Corsiglia [31] observed a change from wakelike vortices to jetlike vortices as a function of angle of attack, where larger angles of attack resulted in jetlike profiles. Giuni and Green [32] further showed that the wing-tip shape could either promote or attenuate the tendency for the vortex to meander within the far field. Similarly, Anderson and Lawton [33] showed that

TABLE I. Vortex quantities

α (°)	D_c (mm)	τ
5	5.8	0.09
10	7.4	0.17

the magnitude of the axial flow within the vortex is influenced by the end conditions. Both Lee and Pereira [30] and Giuni [34] anticipate that this higher-speed peak should dissipate with increasing distance downstream of the generator, although the previously cited literature does indicate that it can persist into the far field.

Additional information can be obtained about the vortices from observing the distributions of vertical velocity shown in Fig. 3(b). The vortex swirl (τ) can be defined as:

$$\tau = \left(\frac{U_\theta}{U_\infty}\right)_{max},\tag{1}$$

where U_θ is the azimuthal velocity and U_∞ is the freestream velocity. Due to this asymmetry, the swirl ratio is determined from the average of the two peaks seen in Fig. 3, according to Kalkhoran and Smart [4]. Table I presents the quantities derived from interrogation of Fig. 3. For each angle of attack, a swirl ratio and a core diameter (D_c) are presented. To provide an estimation for the degree of vortex meander, the vortex core location was estimated from twenty nonconsecutive images. These estimations were performed by simply recording the approximate location where in-plane velocity vectors were minimum [35]. The variations about the core are shown in Fig. 4. From these data, a standard deviation was obtained for each motion. The 5° vortex wonders 0.56 mm in the z direction and 0.39 mm in the y direction. The 10° vortex wonders 0.62 mm in the z direction and 0.37 mm in the y direction. Taking the magnitude of these values, the wondering for the 5° and 10° vortices is 0.68 mm and 0.72 mm, respectively. Referring to the estimations of the core size, this is 11.7% and 9.7% of the 5° and 10° core sizes, respectively.

Beresh *et al.* [36] investigated vortex meander in more detail to ascertain the influence on the measured vortex parameters. Their findings demonstrated that the mean velocity field was largely

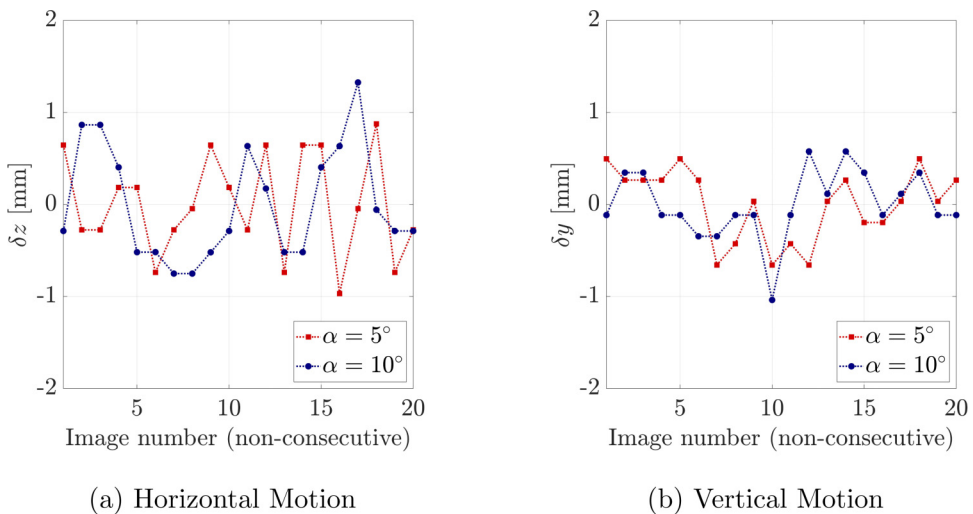(a) Horizontal Motion

(b) Vertical Motion

FIG. 4. Measurement of the motion of the vortex core across 20 nonconsecutive images: (a) horizontal motion and (b) vertical motion.

insensitive to the meander, with a greater measurable influence on the turbulence quantities. One example of what they saw as an influence of meander was a large amount of turbulence kinetic energy focused within the core of the vortex; on applying a correction, the core exhibited greatly reduced quantities in comparison. It is believed here that the flow feature with the most sensitivity to meander will be the reported turbulence kinetic energies. While this may impact the absolute value of the turbulence kinetic energy shown in these data, it should not change comparisons between the cases shown subsequently.

To better illustrate the presence of the vortex, color contours of streamwise vorticity were determined, shown in Fig. 5(a) and Fig. 5(b), where values of $|\omega_x c/U_\infty| < 1$ have been set equal to zero to reduce the presence of noise. Figure 5(a) shows the $\alpha = 5°$ vortex, with a small region of positive (red) vorticity around the origin of the coordinate axis. The main wing-tip vortex is thin and stretched compared to its $\alpha = 10°$ counterpart. Both vortices induce a region of shear with opposite sense above the vortex. For example, in Fig. 5(a), there appears to be a counter-rotating vortex pair around $y/c \approx 0.1$. Although the $\alpha = 10°$ vortex seems to be readily apparent, at least in contrast to the $\alpha = 5°$ vortex, the presence of regions of vorticity make it difficult to distinguish a coherent structure from shear.

Following the determination of the vorticity, a Stk was estimated, which is defined as the particle relaxation time normalized by a characteristic timescale. Recalling that the units of vorticity are those of inverse time, the (ensemble-average) Stokes number was estimated as:

$$\text{Stk} = \tau_p \left(\frac{\partial W}{\partial y} - \frac{\partial V}{\partial z} \right), \tag{2}$$

where τ_p is the particle relaxation time, previously measured across an oblique shock [20]. It was found that Stk appears to be largest within the shear of the vortex, reaching a maximum value of about 0.4. This value decreased rapidly away from the vortex shear toward 0 in the freestream. Returning to the discussion by Lecuona *et al.* [25], the core of the vortex will suffer the most in terms of particle entrainment. As a result, some particle lag is likely present, with an anticipated maximum error around 4%, within the average images, at the vortex core [37,38].

One question that arises from the data in Fig. 5(a) and Fig. 5(b) is whether these are true vortices rather than simply regions of vorticity. To answer this question, the Q_D criterion was applied as a technique for vortex identification. The Q_D criterion is similar in concept to the Q criterion for incompressible flows [39–41]. The incompressible Q criterion takes the difference between the Euclidean norm of the antisymmetric vorticity matrix ($\boldsymbol{\Omega}$) and the norm of the strain matrix ($\mathbf{S}$), identifying a vortical structure as being a region where vorticity is much larger than the strain rate, i.e.:

$$Q = \tfrac{1}{2}(\|\boldsymbol{\Omega}\|^2 - \|\mathbf{S}\|^2) > 0. \tag{3}$$

For an incompressible flow, Eq. (3) is equal to the second invariant of the deformation-rate tensor [40], given as:

$$I_2 = \frac{1}{2}\left[\left(\frac{\partial U_i}{\partial x_i} \right)^2 - \frac{1}{2} \frac{\partial U_i}{\partial x_j} \frac{\partial U_j}{\partial x_i} \right]. \tag{4}$$

Equation (4) is given in its most general form, which allows for application to volumetric data. For two-dimensional data sets, such as those obtained by 3-component PIV, this equation reduces to a form that sets all out-of-plane derivatives equal to zero; for this reason, the indices here are $i = 1$, 2. The equality of Eq. (3) and Eq. (4) is only strictly true for an incompressible flow, for which the volumetric strain rate is zero. To correct for the contribution of a nonzero volumetric strain rate, Kolar [40] recommends the following formulation (for 2D flows) based on the use of the deviatoric component of $\mathbf{S}$:

$$Q_D = \frac{1}{2}\left[\|\boldsymbol{\Omega}\|^2 - \left\| \mathbf{S} - \frac{1}{3}\text{tr}(\mathbf{S})\mathbf{I} \right\|^2 \right], \tag{5}$$

(a) $\alpha = 5°$

(b) $\alpha = 10°$

(c) $\alpha = 5°$

(d) $\alpha = 10°$

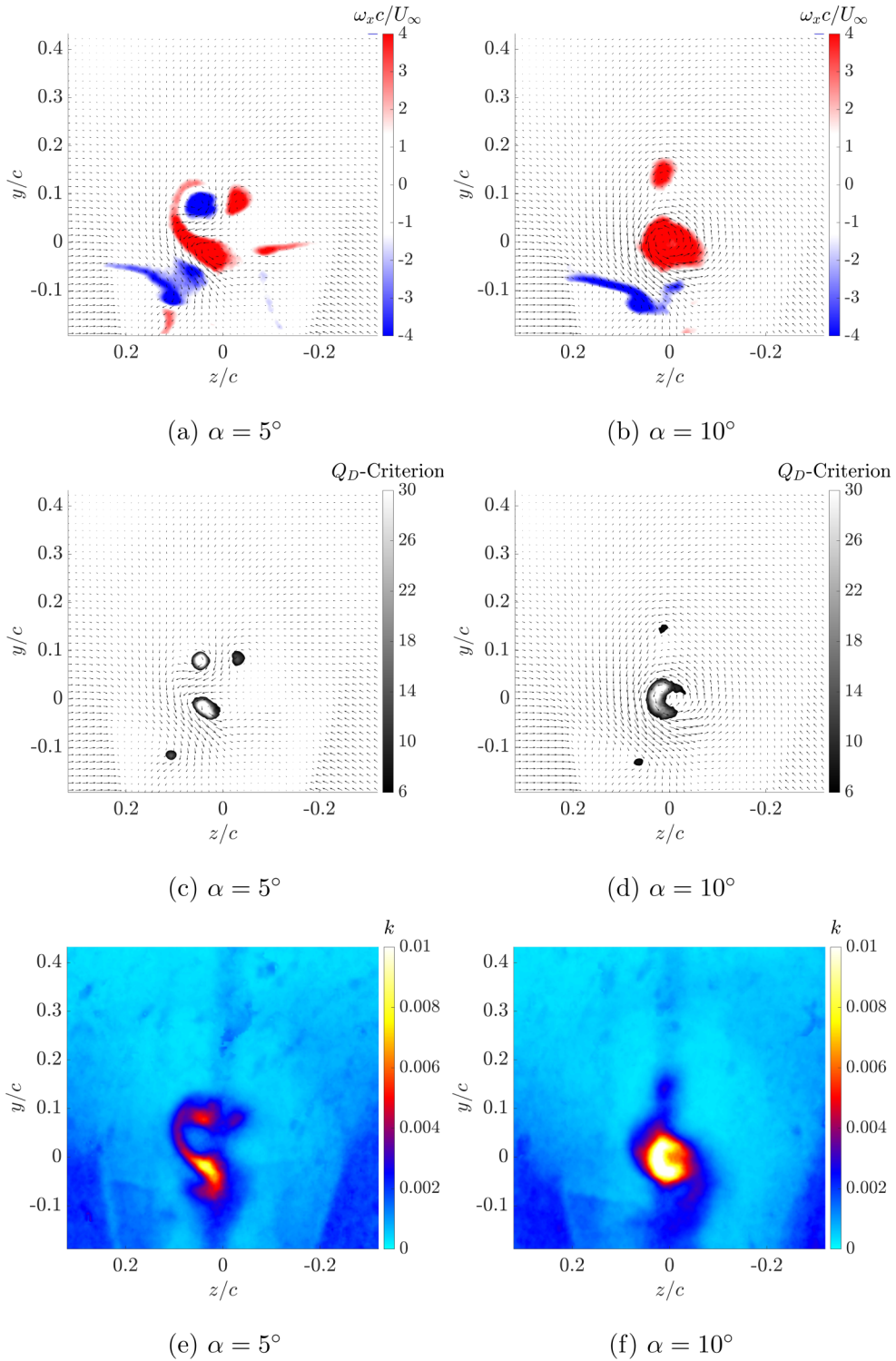(e) $\alpha = 5°$

(f) $\alpha = 10°$

FIG. 5. Color contours of streamwise vorticity [(a) and (b)], Q_D criterion [(c) and (d)], and turbulence kinetic energy [(e) and (f)] for the vortex, obtained at $x/c = 1.5$.

TABLE II. Postshock total velocity ($V_{\text{tot},2}/U_\infty$)

θ (°)		P_2/P_1	$V_{\text{tot},2}/U_\infty$		$\Delta V_{\text{tot},2}$
Design	Actual	Theory	Theory	SPIV	(%)
15	14.5	2.67	0.85	0.85	0.00
20	18.3	3.34	0.80	0.82	2.50
25	22.4	4.17	0.76	0.75	1.32

where $\mathbf{I}$ is the identity matrix and tr designates the trace of the matrix. Contours of $Q_D > 6$ are given in Fig. 5(c) and Fig. 5(d) for the two angles of attack. For $\alpha = 5°$, a weaker secondary vortex appears above the main vortex; the presence of such secondary structures has been seen in previous literature within the near-field region of a wing-tip vortex [32]. In contrast, the $\alpha = 10°$ case results in the formation of a single, relatively, large structure.

Figure 5 also shows contours of turbulence kinetic energy, k, which is defined in this case as:

$$k = \frac{1}{2} \sum_{i=1}^{3} \frac{\overline{u_i' u_i'}}{U_\infty^2}. \tag{6}$$

The quantity, u_i', is the fluctuating component of velocity obtained from Reynolds decomposition, which does not distinguish between random and coherent motion. In both instances, k is primarily focused within the vortex itself, albeit asymmetrically about the vortex core. As would be expected, Fig. 5(f) shows a greater amount of k for the $\alpha = 10°$ vortex, compared to the $\alpha = 5°$ vortex seen in Fig. 5(e). These regions of large k appear to coincide with the vortical structures identified within Fig. 5(c) and Fig. 5(d), further providing evidence that these are distinct vortical structures.

B. Centerline measurements of oblique shock-vortex interactions

Having quantified the incoming vortices, it is now possible to investigate the interaction in detail using planar measurements. The following sections first quantify the baseline shocks used in this study before assessing the influence of the vortices on the flow field. The baseline oblique shock measurements were obtained without the airfoil present within the test section. This was done for several reasons: (1) to quantify the original oblique shock as best as possible and show how closely these data agree with theoretical values and (2) to show how the shock changes due to the presence of the airfoil. In contrast, the vortex cases are measured with the airfoil present.

1. Baseline planar measurements

Centerline measurements of the baseline shocks are shown in Fig. 6. To assess the possibility of contamination from wave reflections, the baseline data were obtained without the airfoil present. The flow field is presented with color contours of total velocity in Fig. 6(a), Fig. 6(d), and Fig. 6(g); color contours of spanwise velocity in Fig. 6(b), Fig. 6(e), and Fig. 6(h); and color contours of turbulence kinetic energy in Fig. 6(c), Fig. 6(f), and Fig. 6(i). Each image is presented with superposed in-plane velocity vectors (subsampled for clarity) for the cases of $\theta = 15°$, $20°$, and $25°$, where θ is the angle of the shock generator (i.e., wedge) with respect to the freestream. The vector resolution for these images is about 0.27 mm/vector. The black silhouettes represent the wedge itself, in terms of leading edge and upper surface location (not thickness). Each field of view has been rotated; in addition, $x/c = 0$ corresponds to the midchord of the wing, and $y/c = 0$ corresponds to the wing tip. The freestream velocity moves from left to right in these images.

The Mach number seen by the wedge is approximately 2.92, resulting in a freestream velocity of about 620 m/s. To provide faith in the use of the SPIV in quantification of the oblique shock, the measured velocity fields were compared with oblique shock theory, as shown in Table II, where $V_{\text{tot},2}$
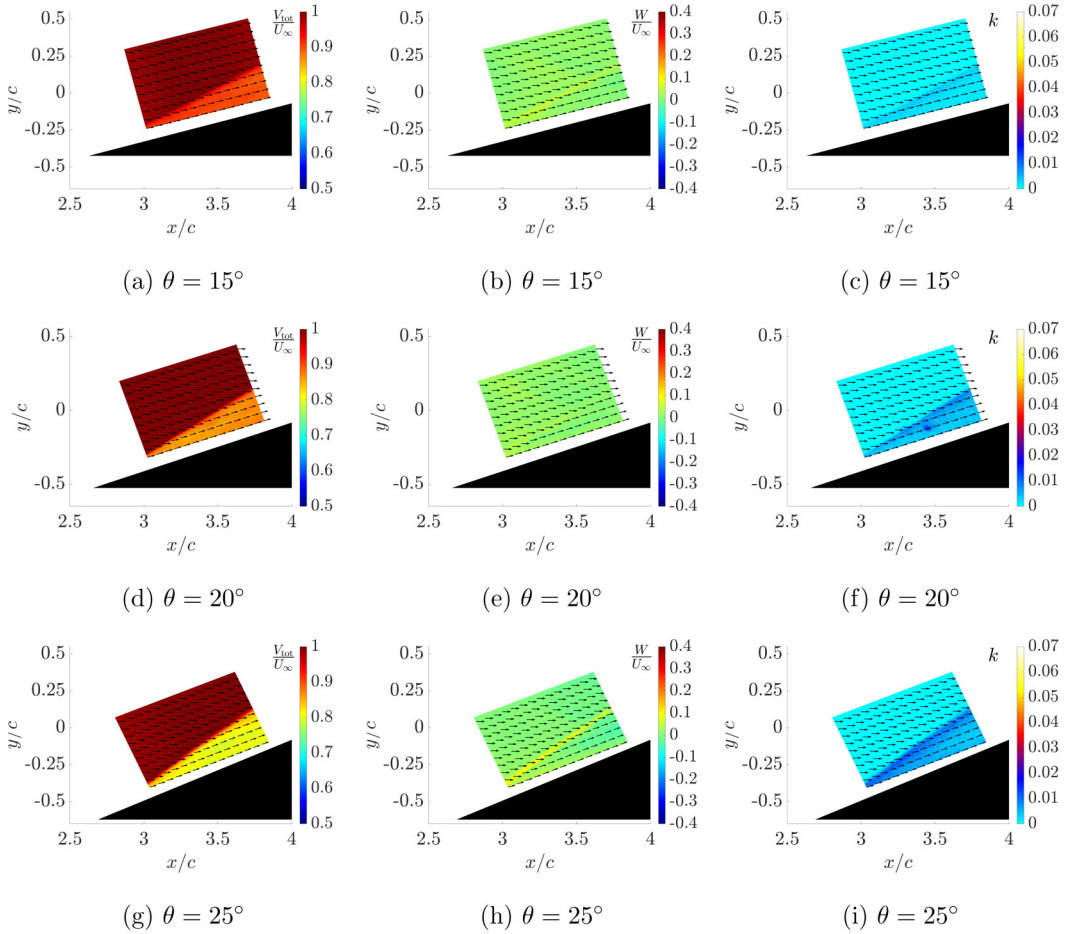
FIG. 6. Color contours of total velocity [(a), (d), and (g)], spanwise velocity [(b), (e), and (h)], and turbulence kinetic energy [(c), (f), and (i)] with in-plane velocity vectors (ensemble average) for the baseline oblique shocks.

represents the total velocity downstream of the oblique shock. It is readily evident that the flow sees slightly different wedge deflection angles than designed; this was determined by rotating the SPIV field of view until a minimum vertical velocity was reported in the freestream. Using these corrected values of θ, the measured values for the downstream total velocity show a maximum error of 2.5% when compared to theory. For the remainder of this paper, the shocks will be referred to based on their designed angles, namely $\theta = 15°, 20°, 25°$, as opposed to the corrected values. In addition, the theoretical estimations for the static pressure jump across each shock are also presented in Table II, where P_1 and P_2 are the static pressures upstream and downstream of the shock, respectively.

A two-dimensional oblique shock is readily apparent for each deflection angle, as indicated in Fig. 6(a), Fig. 6(d), and Fig. 6(g) from the sharp change in total velocity. As the deflection angle increases, a larger decrease in the postshock total velocity is seen in Fig. 6, matching expectations regarding the strength of the shock. The vector field shows velocity vectors suddenly change direction due to the influence of the shock, such that flow remains parallel to the wedge surface. Observing the spanwise velocity contours in Fig. 6(b), Fig. 6(e), and Fig. 6(h), a nearly zero spanwise velocity is evident in each case, demonstrating that two-dimensional flows were achieved within the ensemble-average measurements.

Appreciable nonzero values of spanwise velocity are present in a thin line about the shock. A bias uncertainty is associated with viewing through the shock, which is apparent from the presence of these increased levels of spanwise velocity at the location of the shock. This is likely associated with optical distortions due to the large density gradient at the location of the shock. As discussed by Scarano [42], one uncertainty associated with viewing across a shock is the apparent blurring of particles, which can give rise to wider and skewed correlation peaks. In addition, Elsinga and Orlicz [43] demonstrated that viewing a shock even at an angle of greater than $5°$ can give rise to increased uncertainties, which would be compounded with a SPIV system, particularly if one camera is viewing from the low-density side of the shock. As Lang *et al.* [44] illustrates, uncertainties are larger for the spanwise velocity component. Because this would be assumed to be a bias uncertainty, it would not be represented from the precision uncertainty estimates. Further, as can be seen from the averaged images, the spanwise velocity rapidly decays to the expected value away from the shock. Note finally that the thickness of the shock is not realistic in these images; due to blurring and particle lag, the shock will appear to be thicker than it really is.

Looking at the contours of turbulence kinetic energy, the freestream continues to have negligibly small levels near zero. Note that the levels of k in Fig. 6 are different from those shown in Fig. 5; i.e., the scale in Fig. 6 is larger by a factor of five. Downstream of the shock, the turbulence kinetic energy increases slightly as a function of shock angle; specifically, Fig. 6(i) shows the largest values of k. In general, Fig. 6 demonstrates that the spanwise velocity and turbulence kinetic energy is either zero or very small within the baseline flow fields; providing not only evidence of the quality of these data but will also serve to demonstrate changes to the flow field under the influence of the streamwise vortex impingement.

2. Planar measurements of the interactions

The interactions of the three wedge angles with the $\alpha = 5°$ streamwise vortex are shown in Fig. 7, which presents the data as color contours of total velocity, spanwise velocity, and turbulence kinetic energy, along with superposed in-plane velocity vectors at a subsampled vector density. The data are presented in the same manner as shown in Fig. 6 to facilitate comparisons with their respective baselines. It is expected that the vortex will not travel in a straight line from the wing tip. The OSVI data shown in this section indicate evidence that the vortex moved inboard, due to the point of impingement being below the free-end of the wing.

The total velocity contours are shown in Fig. 7(a), Fig. 7(d), and Fig. 7(g). The location of the vortex impingement appears to be around $y/c \approx -0.2$, relatively close to the wedge surface. Looking at the Schlieren images obtained by Kalkhoran and Sforza [16] and Smart *et al.* [18], along with the simulations of Rizzetta [9], the wing tip vortex issues from the free-end and moves slightly inboard with increasing streamwise distance. This is likely due to the presence of a low pressure wake downstream of the wing drawing flow inboard. As $y/c = 0$ corresponds to the free-end of the wing, it is apparent that the core of the vortex did in fact move slightly inboard. Compared to the baseline, no major changes to the shape of the shock are observable, which readily indicates these measurements correspond to the classical definition of a weak interaction.

Within the postshock regions in Fig. 7(a), Fig. 7(d), and Fig. 7(g), a noticeable decrease in total velocity is seen in all three cases, close to the wedge surface. With increasing distance away from the wedge surface, the postshock velocity increases, nearly approaching values seen in the baseline cases in Fig. 6. Decreased total velocity implies a relative increase in static pressure under energy conservation, indicating that even a relatively weak vortex can alter the flow field about the wedge. Furthermore, no evidence of reverse axial flow is evident within any of these vector fields.

The spanwise velocity components, seen in Fig. 7(b), Fig. 7(e), and Fig. 7(h), show more dramatic changes under the influence of the $\alpha = 5°$ vortex. It is assumed that the presence of spanwise velocity is indicative of the presence of rotational motion. Furthermore, the presence of these nonzero spanwise velocities is not evidence of measurement bias as no comparable levels were detected within the baseline, as seen previously in Fig. 6. Finally, the turbulence kinetic energy
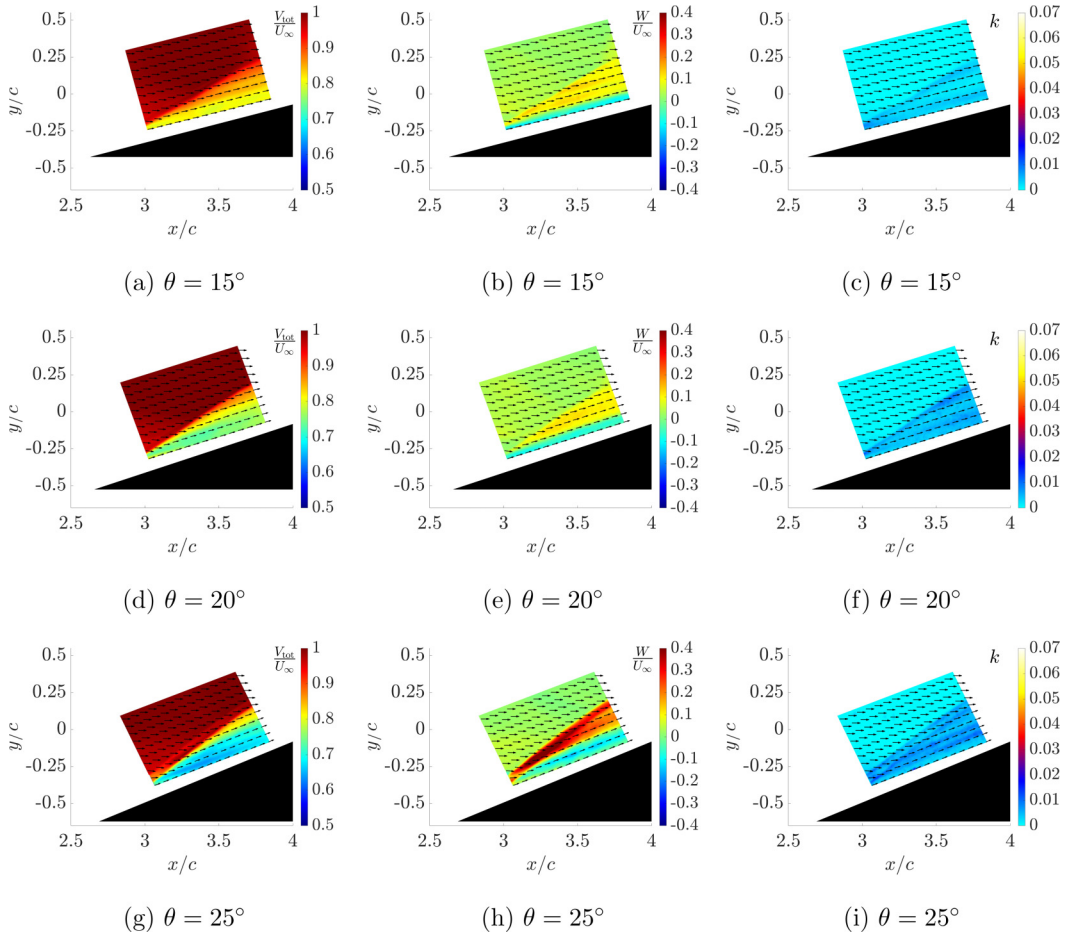
FIG. 7. Color contours of total velocity [(a), (d), and (g)], spanwise velocity [(b), (e), and (h)], and turbulence kinetic energy [(c), (f), and (i)] with in-plane velocity vectors (ensemble-average) for $\alpha = 5°$ interaction.

contours show little influence from the vortex impingement, with levels barely different from the baseline.

More dramatic changes appear under the influence of the $\alpha = 10°$ vortex, as shown in Fig. 8. Across Fig. 8(a), Fig. 8(d), and Fig. 8(g), the postshock velocity has a large scale decrease compared to Fig. 7, which is likely associated with the larger axial velocity deficit within the $\alpha = 10°$ vortex. In all three cases, the shape of the shock has also changed; this is evident by the enlarged postshock flow region compared to those seen in Fig. 7. The shocks appear to be elevated above the surface of the wedge. In addition, Fig. 8(g) shows the largest changes, where the shock develops a noticeable curvature at the point of interaction with the oncoming vortex. None of the three cases in Fig. 8 appear to show evidence of reverse axial flow. For these reasons, the flow fields visualized here demonstrate at least one moderate interaction.

The spanwise velocity contours for the $\alpha = 10°$ vortex are shown in Fig. 8(b), Fig. 8(e), and Fig. 8(h). Similarly to what was seen previously, the spanwise velocity is associated with the azimuthal velocity about the incoming vortex. One thing that is interesting in the $\alpha = 10°$ interactions is the increased level of spanwise velocity found within the freestream. This is not a measurement error, given that these elevated levels were not present within either the baseline or
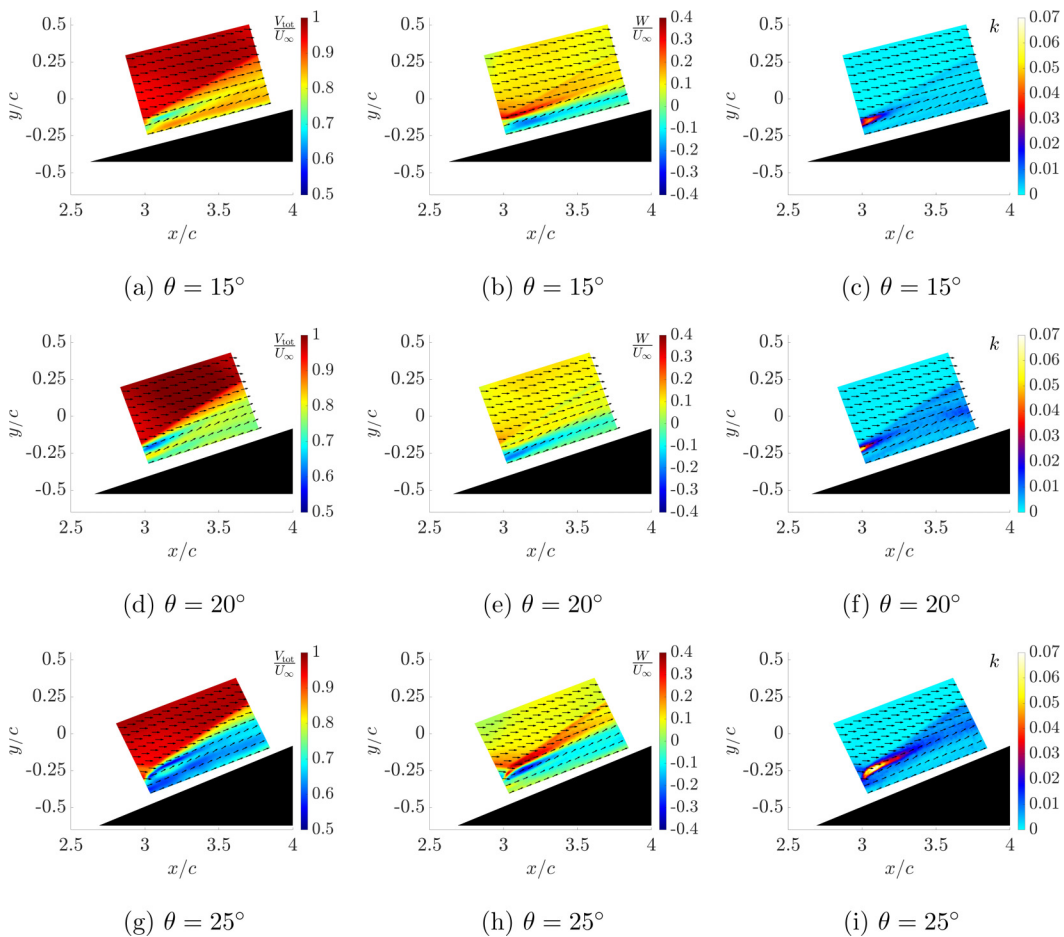
FIG. 8. Color contours of total velocity [(a), (d), and (g)], spanwise velocity [(b), (e), and (h)], and turbulence kinetic energy [(c), (f), and (i)] with in-plane velocity vectors (ensemble-average) for $\alpha = 10°$ interaction.

the $\alpha = 5°$ cases. As will be discussed subsequently, this is attributed to being due to the wake downstream of the pitched wing.

Levels of turbulence kinetic energy appear to be increased in all three interactions shown in Fig. 8(c), Fig. 8(f), and Fig. 8(i), as evidenced by the darker blue contours. As the vortex passes through the shock, increased turbulent mixing appears to arise, leading to these larger values. Additionally, a large increase in k is seen in all three cases, near the location where the vortex impinges on the shock. Note that turbulence kinetic energy represents the kinetic energy associated with velocity fluctuations. The increases seen here could be indicative of increased levels of unsteadiness apparent within the flow field. Unsteadiness within moderate interactions has been observed by several researchers within the past, although little data have been presented demonstrating this [4]. For example, Leopold *et al.* [5] reported unsteadiness within their LDV data. Kalkhoran and Sforza [16] similarly reported noticing unsteadiness within the interaction; however, only time-averaged values were provided. The resolution of increased turbulence kinetic energy levels in these data, surrounding the point of vortex impingement, is a unique element.

(a) $\theta = 15°, x/c = 3.2$

(b) $\theta = 15°, x/c = 3.4$

(c) $\theta = 15°, x/c = 3.6$

(d) $\theta = 20°, x/c = 3.2$

(e) $\theta = 20°, x/c = 3.4$

(f) $\theta = 20°, x/c = 3.6$

(g) $\theta = 25°, x/c = 3.2$

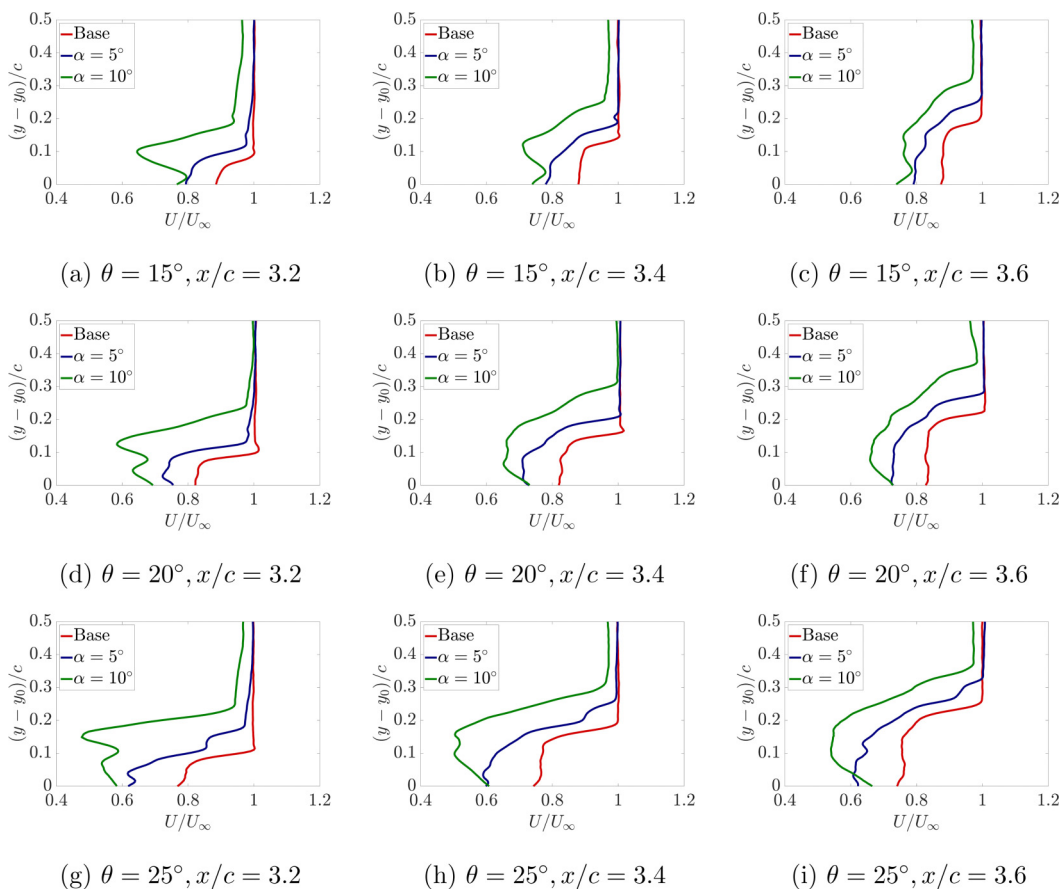(h) $\theta = 25°, x/c = 3.4$

(i) $\theta = 25°, x/c = 3.6$

FIG. 9. Distributions of streamwise velocity downstream of the shock. The value y_0 represents the lower limit of the data set.

3. Wall-normal velocity distributions

Wall-normal distributions (with respect to the wind tunnel's floor) of the streamwise, vertical, and spanwise velocity components are presented in Fig. 9, Fig. 10, and Fig. 11, respectively. To obtain these distributions, the scattered SPIV data were interpolated, using Matlab's scatteredInterpolant function, along lines parallel to the y axis, as defined in Fig. 1. Because these distributions were created from an interpolation process, they are presented here as smooth lines as opposed to discrete data points; therefore the original vector resolution is not well represented by these figures, although the trends are. As stated above, the original vector resolution is 0.27 mm/vector; this value was used as the grid resolution for creating these interpolations, although the rotated image will have a slightly reduced vector resolution along the rotated vertical and horizontal directions. In addition, the vertical distance, y, is presented as a relative distance from the bottom edge of the data set (y_0).

The streamwise velocity profiles in Fig. 9 help to highlight some more features of the OSVI that are not as readily apparent from Fig. 7 and Fig. 8. The presence of the shock is evident from the sudden change from the nearly uniform streamwise velocity, which rapidly decreases with decreasing y. Furthermore, the influence of the shock angle can be seen due to the increasing height in this sudden change with increasing streamwise distance. The baseline indicates a nearly uniform flow downstream of the shock; the two OSVI cases, on the other hand, show postshock regions with increased velocity deficits. For the $\alpha = 10°$ case, this deficit slightly resembles the profile seen
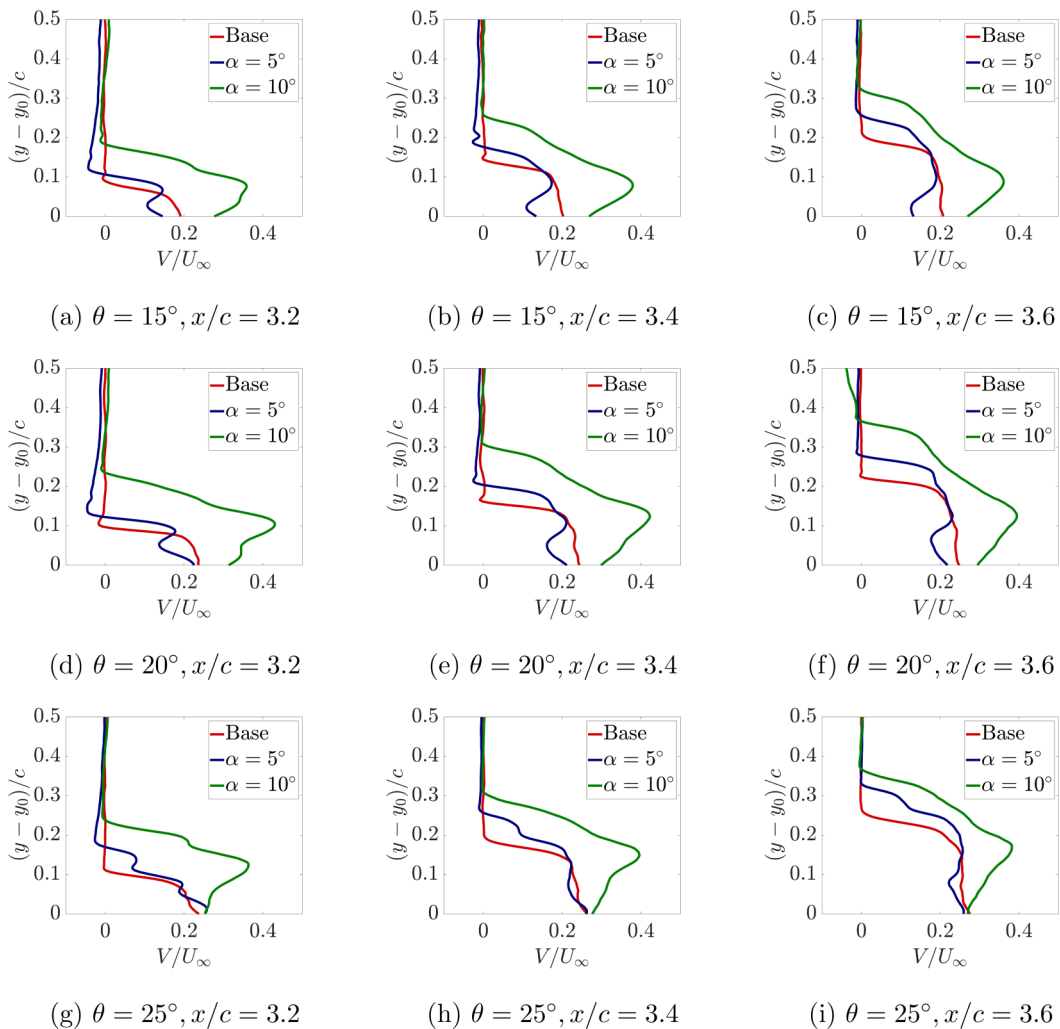
FIG. 10. Distributions of vertical velocity downstream of the shock. The value y_0 represents the lower limit of the data set.

in Fig. 3(a) in terms of shape. In addition, the velocity deficit appears to grow with shock angle, although the same vortices were used in each case.

Within the $\theta = 15°$ profiles in Fig. 9(a), Fig. 9(b), and Fig. 9(c), the baseline and the $\alpha = 5°$ case nearly collapse on top of each other within the freestream while showing differences within the postshock region. This trend appears to continue across all wedge angles, with each wedge angle demonstrating increasing velocity deficits downstream of the shock. The $\alpha = 10°$ case, however, never collapses on top of the other two cases within the freestream. This can be seen across all wedge angles. At first, this appears to be a potential error in the measurement; however, referring to Fig. 5, it can be seen that the flow downstream of the wing develops into a wake structure. The wake of the $\alpha = 5°$ vortex has a slightly smaller velocity deficit than the $\alpha = 10°$ vortex. In addition, as the $\alpha = 10°$ has a larger swirl value, it induces a greater spanwise velocity. This induced spanwise velocity will be evident subsequently, with a hint of its presence already apparent in Fig. 8, across the spanwise velocity contours. It would appear that the wake of the $\alpha = 5°$ vortex diffuses more
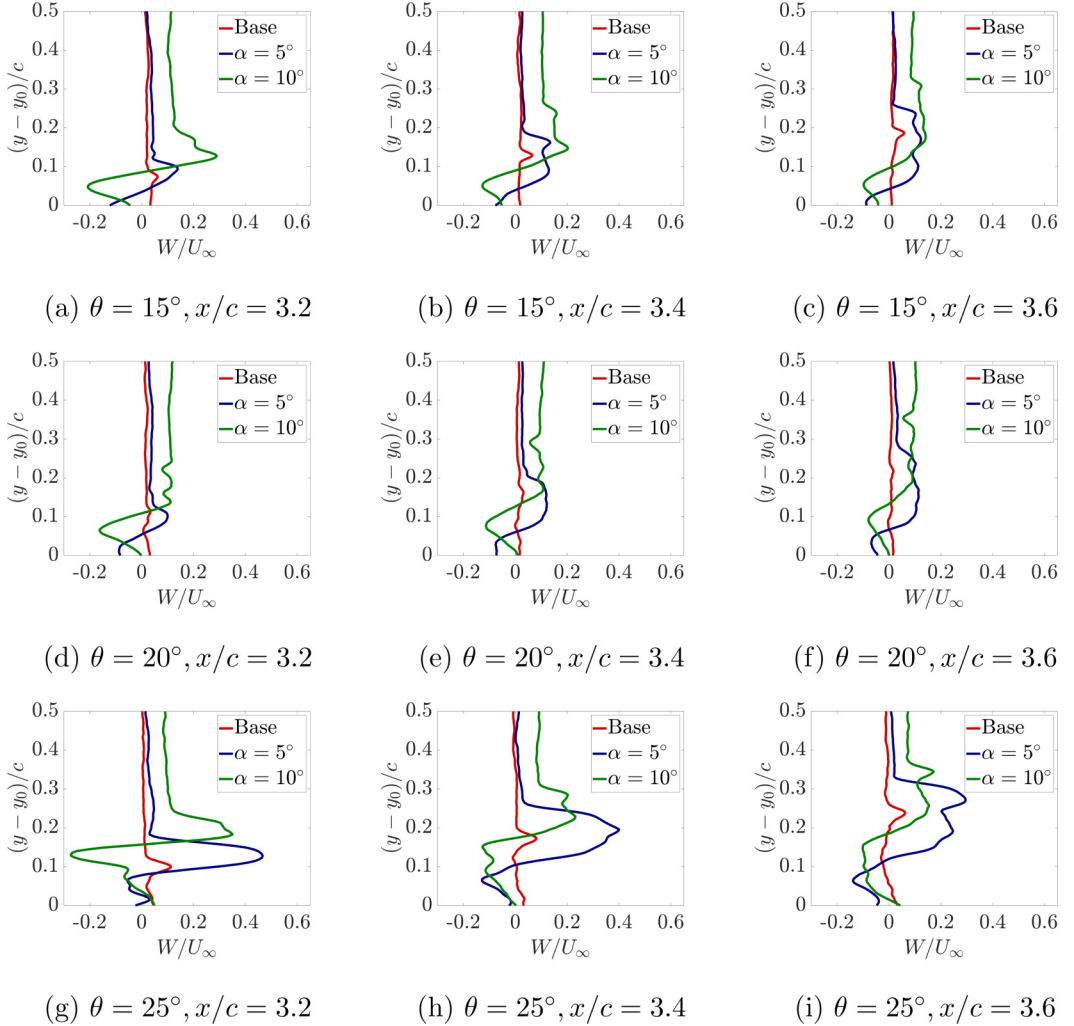
FIG. 11. Distributions of spanwise velocity downstream of the shock. The value y_0 represents the lower limit of the data set.

rapidly than the $\alpha = 10°$ vortex; the $\alpha = 10°$ cases still show a reduced freestream compared to the baseline and $\alpha = 5°$ cases seen in Fig. 9.

One additional observation that is apparent from Fig. 9 is that the $\alpha = 5°$ interactions all result in a slight change to the position of the shock in all cases. This is an interesting result in that even a weak interaction still contributes some alteration to the shock structure itself, which was observed within the simulations of Magri and Kalkhoran [10], but tends to be less obvious from Schlieren imaging. Combined with the measurable difference in the velocity deficit downstream of the shock, it can be clearly seen that even the weak interaction results in an alteration to the flow field about the wedge.

The distributions of vertical velocity, shown in Fig. 10, provide similar insight into the interaction flow field. Upstream of the shock wave, vertical velocity is nearly zero, as expected; this is true in all cases. Comparing across the cases, the baseline and the $\alpha = 5°$ interactions have nearly identical distributions in vertical velocity downstream of the shock, with the primary difference being a noticeable change in the shock location. The $\alpha = 10°$ interaction, on the other hand, shows

a dramatic increase in vertical velocity downstream of the shock. Distributions of spanwise velocity are shown in Fig. 11. The data shown thus far were obtained at a spanwise location estimated to be the centerline of the incoming vortex. It is anticipated that a trace in the spanwise velocity should therefore show two peaks: a positive and a negative, which would be associated with the induced velocity of the vortex. This pattern is best exemplified by the green trend in Fig. 11(g), which corresponds to the $\alpha = 10°$ interaction on the $\theta = 25°$ wedge.

In general, the $\theta = 15°$ and $20°$ shocks tend to show rather similar levels of spanwise velocity across all three streamwise locations. In contrast, the $\theta = 25°$ cases appear to show increased levels of spanwise velocity that are greater than anticipated. Note that the azimuthal velocity, which was locally equal to the vertical velocity in Fig. 3, indicated peak values of $V < 0.2U_\infty$. The values shown in Fig. 11(g), Fig. 11(h), and Fig. 11(i) are much greater. This may be due to the higher levels of uncertainty found in the spanwise velocities of the interaction, as indicated within the Experimental Setup. Nevertheless, it is expected that qualitatively, these trends represent flow features induced by the passage of the vortex through the shock.

Another interesting item to comment on is the increased levels of spanwise velocity seen for $\alpha = 10°$, across all wedge deflections, outside of the shock, within the freestream. These were particularly noticeable in Fig. 8. Similarly to the streamwise velocity distributions in Fig. 9, at first glance this would appear to be a bias in the data. Referring to Fig. 2(b), however, the $\alpha = 10°$ vortex induces a strong spanwise velocity component in the same direction as seen in Fig. 11; the result is a similar influence seen in the streamwise velocity components in Fig. 9.

IV. CONCLUSIONS

Experiments have been performed at Rutgers University to quantify the interaction of a wing-tip vortex with an oblique shock, using stereoscopic particle image velocimetry. The vortex was formed using a finite wing pitched to one of two angles of attack: $5°$ and $10°$. Both angles resulted in wakelike vortices, with swirl ratios measured to be $\tau = 0.09$ and 0.17, respectively. A wedge was placed approximately $2.6c$ downstream of the wing, producing an oblique shock. Three oblique shocks were used in this study, with nominal deflection angles of $\theta = 15°$, $20°$, and $25°$. The interactions with the $\alpha = 5°$ vortex resembled those of the classically defined weak type, whereby little change was induced to the shape of the shock and the vortex appeared to persist downstream. In contrast, the interactions with the $\alpha = 10°$ vortex seemed to be moderate, resulting in deformation of the shock but without the discernible presence of reverse axial flow and no distinct signs of immediate vortex breakdown.

Regardless of interaction type, all cases exhibited increased velocity deficits downstream of the shock due to the influence of the vortex. In the case of $\alpha = 10°$, this leads to increased mixing above that found in the baseline. This was particularly strong at the location of vortex impingement on the shock, where high regions of turbulence kinetic energy imply the existence of increased unsteadiness in comparison to the $\alpha = 5°$ cases. Passage of the vortex through the shock also leads to the formation of spanwise motion, which persisted in all cases. Even in the weak case, a slight shift in the shape of the shock was observable from line distributions of velocity. Evidence within these data indicate that vortex breakdown did not occur immediately downstream of the shock.

[1] J. M. Delery, Aspects of vortex breakdown, Prog. Aerosp. Sci. **30**, 1 (1994).

[2] S. J. Beresh, J. A. Smith, J. F. Henfling, T. W. Grasser, and R. W. Spillers, Interaction of a fin trailing vortex with a downstream control surface, AIAA Paper No. 2008-0342 (AIAA, Reston, VA, 2008).

[3] D. J. Lesieutre and O. Quijano, Studies of vortex interference associated with missile configuration, AIAA Paper No. 2014-0213 (AIAA, Reston, VA, 2014).

[4] I. M. Kalkhoran and M. K. Smart, Aspects of shock wave-induced vortex breakdown, Prog. Aerosp. Sci. **36**, 63 (2000).

[5] F. Leopold, F. Jagusinski, and C. Demeautis, Experimental investigation of shock/vortex interaction for slender canard configurations at supersonic speed, in *20th International Congress on Instrumentation in Aerospace Simulation Facilities, 2003, ICIASF '03* (IEEE, Gottingen, Germany, 2003), pp. 247–257.

[6] M. K. Smart and I. M. Kalkhoran, Effect of shock strength on oblique shock-wave/vortex interaction, AIAA J. **33**, 2137 (1995).

[7] M. K. Smart, I. M. Kalkhoran, and S. Popovic, Some aspects of streamwise vortex behavior during oblique shock wave/vortex interaction, Shock Waves **8**, 243 (1998).

[8] T. Hiejima, Criterion for vortex breakdown on shock wave and streamwise vortex interactions, Phys. Rev. E **89**, 053017 (2014).

[9] D. P. Rizzetta, Numerical simulation of oblique shock-wave/vortex interaction, AIAA J. **33**, 1441 (1995).

[10] V. Magri and I. M. Kalkhoran, Numerical investigation of oblique shock wave/vortex interaction, Comput. Fluids **86**, 343 (2013).

[11] J. M. Delery, E. Horowitz, O. Leuchter, and J. L. Solignac, Fundamental studies on vortex flows, Rech. Aerosp. **2**, 1 (1984).

[12] L. N. Cattafesta and G. S. Settles, Experiments on shock/vortex interaction, in *Proceedings of the 30th Aerospace Sciences Meeting and Exhibit*. AIAA Paper 92-0315 (AIAA, Reston, VA, 1992).

[13] O. Metwally, G. Settles, and C. Horstman, An experimental study of shock wave/vortex interaction, in *Proceedings of the 27th Aerospace Sciences Meeting*. AIAA Paper 89-0082 (AIAA, Reston, VA, 1989).

[14] T. O. Klaas and W. Schroder, Oblique shock-vortex interaction, Proc. Appl. Math. Mech. **2**, 334 (2003).

[15] I. M. Kalkhoran, P. M. Sforza, and F. Y. Wang, Experimental study of shock-vortex interaction in a Mach 3 stream, in *Proceedings of the 9th Applied Aerodynamics Conference*. AIAA Paper 91-3270 (AIAA, Reston, VA, 1991).

[16] I. M. Kalkhoran and P. M. Sforza, Airfoil pressure measurements during oblique shock wave/vortex interaction in a Mach 3 stream, AIAA J. **32**, 783 (1994).

[17] M. Klaas, W. Schroder, and W. Althaus, Experimental investigation of slender streamwise vortices and oblique shock-vortex interaction, in *Proceedings of the 35th AIAA Fluid Dynamics Conference and Exhibit*. AIAA Paper 2005-4652 (AIAA, Reston, VA, 2005).

[18] M. K. Smart, I. M. Kalkhoran, and J. Bentson, Measurements of supersonic wing tip vortices, AIAA J. **33**, 1761 (1995).

[19] B. Wieneke, Piv uncertainty quantification from correlation statistics, Meas. Sci. Technol. **26**, 074002 (2015).

[20] R. B. Panco and E. P. DeMauro, Measurements of a Mach 3.4 turbulent boundary layer using stereoscopic particle image velocimetry, Exp. Fluids **61**, 107 (2020).

[21] O. Thomer, M. Klaas, and W. Schröder, Oblique shock-vortex interaction, in PAMM: *Proceedings in Applied Mathematics and Mechanics* (WILEY-VCH Verlag, Berlin, 2003), Vol. 2, pp. 334–335

[22] K. Mahesh, A model for the onset of breakdown in an axisymmetric compressible vortex, Phys. Fluids **8**, 3338 (1996).

[23] V. Borisov, A. Davydov, T. Konstantinovskaya, A. Lutsky, A. Shevchenko, and A. Shmakov, Numerical and experimental investigation of a supersonic vortex wake at a wide distance from the wing, in *AIP Conference Proceedings* (AIP, Melville, NY, 2018), Vol. 2027, p. 030120.

[24] D. P. Rizzetta, Numerical investigation of supersonic wing-tip vortices, AIAA J. **34**, 1203 (1996).

[25] A. Lecuona, U. Ruiz-Rivas, and J. Nogueira, Simulation of particle trajectories in a vortex-induced flow: Application to seed-dependent flow measurement techniques, Meas. Sci. Technol. **13**, 1020 (2002).

[26] D. M. Birch and N. Martin, Tracer particle momentum effects in vortex flows, J. Fluid Mech. **723**, 665 (2013).

[27] K. T. Christensen, The influence of peak-locking errors on turbulence statistics computed from PIV ensembles, Exp. Fluids **36**, 484 (2004).

[28] D. Michaelis, D. R. Neal, and B. Wieneke, Peak-locking reduction for particle image velocimetry, Meas. Sci. Technol. **27**, 104005 (2016).

[29] W. J. Devenport, M. C. Rife, S. I. Liapis, and G. J. Follin, The structure and development of a wing-tip vortex, J. Fluid Mech. **312**, 67 (1996).

[30] T. Lee and J. Pereira, Nature of wakelike and jetlike axial tip vortex flows, J. Aircraft **47**, 1946 (2010).

[31] N. A. Chigier and V. R. Corsiglia, Wind-tunnel studies of wing wake turbulence, J. Aircraft **9**, 820 (1972).

[32] M. Giuni and R. B. Green, Vortex formation on squared and rounded tip, Aerosp. Sci. Technol. **29**, 191 (2013).

[33] E. A. Anderson and T. A. Lawton, Correlation between vortex strength and axial velocity in a trailing vortex, J. Aircraft **40**, 699 (2003).

[34] M. Giuni, Formation and Early Development of Wingtip Vortices, Ph.D. thesis, University of Glasgow, 2013.

[35] H. Igarashi, P. A. Durbin, H. Ma, and H. Hu, A stereoscopic PIV study of a near-field wingtip vortex, in *Proceedings of the 48th AIAA Aerospace Sciences Meeting Including the New Horizons Forum and Aerospace Exposition*. AIAA Paper No. 2010-1029 (AIAA, Reston, VA, 2010).

[36] S. J. Beresh, J. F. Henfling, and R. W. Spillers, Meander of a fin trailing vortex and the origin of its turbulence, Exp. Fluids **49**, 599 (2010).

[37] S. J. Beresh, J. F. Henfling, and R. W. Spillers, Time-resolved planar velocimetry of the supersonic wake of a wall-mounted hemisphere, AIAA J. **57**, 1383 (2019).

[38] M. Samimy and S. K. Lele, Motion of particles with inertia in a compressible free shear layer, Phys. Fluids **3**, 1915 (1991).

[39] V. Kolář, Vortex identification: New requirements and limitations, Int. J. Heat Fluid Flow **28**, 638 (2007).

[40] V. Kolar, Compressibility effect in vortex identification, AIAA J. **47**, 473 (2009).

[41] V. Kolář and J. Sistek, Corotational and compressibility aspects leading to a modification of the vortex-identification Q-Criterion, AIAA J. **53**, 2406 (2015).

[42] F. Scarano, Overview of PIV in supersonic flows, in *Particle Image Velocimetry* (Springer, Berlin, 2008), pp. 445–463.

[43] G. E. Elsinga and G. C. Orlicz, Particle imaging through planar shock waves and associated velocimetry errors, Exp. Fluids **56**, 129 (2015).

[44] H. Lang, T. Merck, and J. Woisetchlager, Stereoscopic particle image velocimetry in a transonic turbine stage, Exp. Fluids **32**, 700 (2002).